

## DYNAMICAL AND SPECTRAL MODELING OF THE IONIZED GAS AND NUCLEAR ENVIRONMENT IN NGC 3783

DORON CHELOUCHE<sup>1,2,3</sup> AND HAGAI NETZER<sup>3</sup>

Received 2004 November 4; accepted 2005 February 3

### ABSTRACT

We present a new approach for calculating the physical properties of highly ionized X-ray flows in active galactic nuclei. Our method relies on a detailed treatment of the structure, dynamics, and spectrum of the gas. A quantitative comparison of our model predictions with the 900 ks *Chandra* HETG X-ray spectrum of NGC 3783 shows the following: (1) The highly ionized outflow is driven by thermal pressure gradients, and radiation pressure force is less important. (2) A full-featured dynamical model that provides a very good fit to the high-resolution X-ray spectrum requires a multiphased flow with a density power spectrum reminiscent of the interstellar medium. (3) Adiabatic cooling is an important factor, and so is an additional heating source that may be related to the apparent multiphase and turbulent nature of the flow. (4) The base of the flow is  $\sim 1$  pc from the central object, in agreement with some, but not all, previous estimates. (5) The mass-loss rate is in the range  $0.01\text{--}0.1 M_{\odot} \text{ yr}^{-1}$ , which is smaller than previous estimates and is on the same order as the mass accretion rate in this object.

*Subject headings:* acceleration of particles — galaxies: Seyfert — ISM: jets and outflows — quasars: absorption lines — X-rays: individual (NGC 3783)

### 1. INTRODUCTION

Highly ionized gas (HIG), also known as a “warm absorber,” was first detected in active galactic nuclei (AGNs) in the early 1980s (Halpern 1984) and was observationally and theoretically investigated in hundreds of papers (see, e.g., Netzer et al. 2003, hereafter N03, and references therein). This component is believed to be photoionized by the central X-ray continuum source and is observed in some 50% of all type I (broad line) AGNs (e.g., George et al. 1998, 2000; Porquet et al. 2004). The poor resolution of the pre-*Chandra* and *XMM-Newton* instruments did not allow full investigation of the HIG properties and its possible relation to the UV outflowing gas (e.g., Crenshaw et al. 1999). The launch of *Chandra* and *XMM-Newton* allowed an in-depth analysis of the spectral properties of this gas component (e.g., Kaastra et al. 2000; Kaspi et al. 2000a; Branduardi-Raymont et al. 2001; Lee et al. 2001; Steenbrugge et al. 2005). X-ray absorption lines were detected in several sources and found to be blueshifted by a few hundred  $\text{km s}^{-1}$  relative to the systemic velocity (although much higher velocities have also been reported; e.g., Chartas et al. 2002).

Detailed photoionization modeling of several AGNs show outflows with a stratified density and temperature structure. Such models are partly phenomenological, since they do not self-consistently account for the flow dynamics. Specifically, such models cannot be used to *predict* the velocity and deduce dynamically related quantities such as the mass-loss rate. This information is crucial for understanding the effect of AGN flows on their environment (e.g., King 2003; Scannapieco & Oh 2004). A more complete approach requires full, self-consistent dynamical, photoionization, and spectral modeling of the flows. Today there are only a few qualitative works of this type (e.g., Arav et al. 1994; Murray et al. 1995; Chelouche & Netzer 2003a, 2003b).

This paper introduces a novel approach for investigating the properties of highly ionized flows. It uses the entire spectral information and employs state-of-the-art photoionization, dynamical, and spectral calculations. We apply this method to the X-ray flow in NGC 3783 and compare our model predictions to the 900 ks *Chandra* HETG spectrum of this source (e.g., Kaspi et al. 2002). The paper is organized as follows: In § 2 we summarize the properties of NGC 3783 and its outflow. In § 3 we use general arguments to distinguish between several plausible dynamical models. Section 4 outlines the new formalism, and § 5 presents the self-consistent solution and shows a detailed comparison with the X-ray spectrum of NGC 3783. We elaborate on the implications of our results in § 6 and summarize the work in § 7.

### 2. THE HIGHLY IONIZED GAS IN NGC 3783

NGC 3783 is a Seyfert 1 galaxy that has been extensively studied in almost all spectral bands. It has been the focus of a large UV and X-ray campaign, with several papers already published (Kaspi et al. 2001, 2002; Behar et al. 2003; Gabel et al. 2003a, 2003b; Krongold et al. 2003; N03). While certainly the best-studied AGN in the X-ray band, NGC 3783 is by no means unique, and its low-resolution *ASCA* spectrum resembles that of other AGNs exhibiting warm absorption features (e.g., George et al. 1998).

The bolometric luminosity of NGC 3783,  $L_{\text{tot}}$ , can be estimated from its 2–10 keV X-ray flux reported by Kaspi et al. (2002) and the spectral energy distribution (SED) presented in N03. This results in  $L_{\text{tot}} \simeq 3 \times 10^{44} \text{ ergs s}^{-1}$ , which we assume to be the long-term average luminosity of the source. The mass of the black hole,  $M_{\text{BH}}$ , has been estimated from reverberation mapping to be  $\sim (3 \pm 1) \times 10^7 M_{\odot}$  and the size of the broad-line region (BLR) to be  $\sim 10^{16} \text{ cm}$  (Peterson et al. 2004; see, however, Kaspi et al. [2000b] for lower values). Assuming solar composition for the gas, we define the Eddington ratio,  $\Gamma \equiv 1.18 L_{\text{tot}}/L_{\text{Edd}}$  (e.g., Chelouche & Netzer 2001), where  $L_{\text{Edd}}$  is the Eddington luminosity. For NGC 3783,  $\Gamma \simeq 0.1$ .

The superb 900 ks *Chandra* HETG X-ray spectrum of NGC 3783 allowed the first in-depth study of its HIG outflow. The

<sup>1</sup> School of Natural Sciences, Institute for Advanced Study, Einstein Drive, Princeton, NJ 08540; doron@ias.edu.

<sup>2</sup> Chandra Fellow.

<sup>3</sup> School of Physics and Astronomy and the Wise Observatory, Raymond and Beverly Sackler Faculty of Exact Sciences, Tel Aviv University, Tel Aviv 69978, Israel; netzer@wise.tau.ac.il.

results were thoroughly discussed by Kaspi et al. (2001, 2002), Krongold et al. (2003), and N03. Here we consider the Kaspi et al. (2002) and N03 results as a basis for our model. The main results of these papers can be summarized as follows: The HIG is outflowing at  $v \sim 1000 \text{ km s}^{-1}$ , and the absorption-line profiles exhibit extended blue wings. The velocity (either centroid or dispersion) does not show significant correlation with ionization level. The HIG consists of at least three distinct ionization components (low, intermediate, and high) whose ionization parameters,  $U_{\text{ox}}$  (defined as the ratio of the photon density in the energy range 0.54–10 keV to the hydrogen number density) are  $\log(U_{\text{ox}}) = (-2.4, -1.2, -0.6)$ , respectively. Each component has a different column density,  $N_{\text{H}}$ , given by  $\log(N_{\text{H}}) = (21.9, 22.0, 22.3)$  for the above three values of  $U_{\text{ox}}$ . The N03 analysis shows that none of the HIG components responded to the large, observed continuum variations. Recombination time arguments suggest, therefore, a lower limit on their distance of (3.2, 0.63, 0.18) pc, respectively. The line-of-sight covering factor of the flow,  $C_{\text{los}}$ , is between 0.7 and 1.0. The global ( $4\pi$ ) covering factor of the flow,  $C$ , obtained from the emission lines is  $\sim 20\%$ . The mass-loss rate,  $\dot{M}$ , was estimated to be  $\sim 75\epsilon C M_{\odot} \text{ yr}^{-1}$ , where  $\epsilon$  is the volume filling factor. For  $\epsilon = 1$ , it exceeds the expected mass accretion rate by roughly 2 orders of magnitude.

### 3. GENERAL MODEL CONSIDERATIONS

Several models have been proposed to qualitatively explain the acceleration of highly ionized gas in AGNs (e.g., Krolik & Begelman 1986; Balsara & Krolik 1993; Königl & Kartje 1994; Bottorff et al. 2000; Chelouche & Netzer 2001). The models we consider here assume that the flow is driven either by radiation pressure force, thermal pressure gradients, or a combination of the two. The equation of motion in this case (assuming that the gravitational force is set by the central black hole; see, however, Schödel et al. 2003) is

$$v \frac{dv}{dr} = \frac{1}{\rho} \left[ \frac{n_e \sigma_T L_{\text{tot}}}{4\pi r^2 c} \left( M - \frac{1}{\Gamma} \right) - \frac{dP}{dr} \right], \quad (1)$$

where  $r$  is the distance from the ionizing source,  $v$  is the velocity,  $\rho$  ( $n_e$ ) is the gas density (electron number density),  $\sigma_T$  is the Thomson cross-section,  $P$  is the thermal pressure [ $P = \rho v_s^2$ , where  $v_s = (2k_B T / \mu m_{\text{H}})^{1/2} \simeq 166(T/10^6 \text{ K})^{1/2} \text{ km s}^{-1}$  and  $\mu m_{\text{H}}$  is the average mass per particle;  $\mu \simeq 0.6$  for fully ionized solar-metallicity gas], and  $M$  is the force multiplier defined as the ratio of the total radiation pressure force to that due to Compton scattering (see Chelouche & Netzer [2003a] and references therein). For the densities associated with the HIG ( $\ll 10^{12} \text{ cm}^{-3}$ ), the ionization structure of optically thin flows depends, to a good approximation, only on  $U_{\text{ox}}$ . In this limit,  $M$  is a function of  $U_{\text{ox}}$  and the optical depth in the line per unit thermal velocity width (e.g., Chelouche & Netzer 2003a).

The modeling scheme considered here combines detailed photoionization and spectral calculations (some aspects of which were discussed by N03) with a simplified treatment of the gas dynamics. As shown below, the unique set of observational constraints allows us to quantitatively investigate, for the first time, which of the aforementioned dynamical models is most relevant to the HIG outflow in NGC 3783.

#### 3.1. Radiation Pressure–driven Flows

Nonrotating radiation pressure–dominated outflows require  $M > \Gamma^{-1}$ . Figure 1 suggests that this condition is difficult to meet for solar-metallicity, optically thin HIG, if we assume the

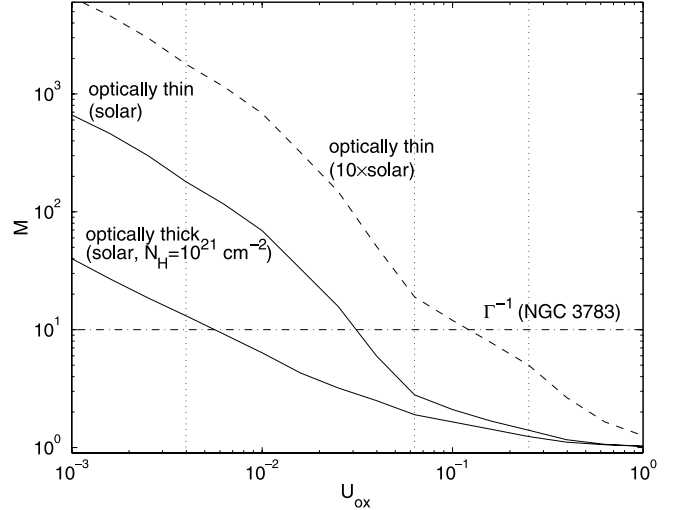


FIG. 1.—Force multiplier,  $M$ , as a function of  $U_{\text{ox}}$  for the SED used by N03. Optically thin and thick (where  $M$  is an average over the cloud) solar-composition gas is shown by solid lines. The gravitational term for NGC 3783 is shown by a horizontal dash-dotted line. The three vertical lines mark the HIG components of N03. Note that unless the flow is highly metal-rich (dashed curve), the radiation pressure force is smaller than gravity for two of the three N03 solutions.

known  $\Gamma$  and SED. Specifically, this condition is not met for the intermediate- and high-ionization components presented in N03, where we find that  $M < \Gamma^{-1}$  for  $U_{\text{ox}} > 5 \times 10^{-3}$ . There is evidence that BLR metallicities can exceed the solar value (e.g., Hamann & Ferland 1993; see, however, Shemmer et al. 2004). In our case, the metallicity should exceed about 30 times solar for the radiation pressure force to overcome gravity for  $U_{\text{ox}} < 0.3$ . Such metallicities have never been observed in AGNs.

Radiation pressure force can exceed gravity close to the footpoint of rotating flows. As shown by Chelouche & Netzer (2001), HIG flows must be launched within or just outside the BLR ( $\sim 10^{16} \text{ cm}$ ) in order to reach the observed velocities. Unless the line broadening in NGC 3783 is unrelated to the gas dynamics, such models cannot account for the width of the line profiles, given the much larger distances implied by the Behar et al. (2003) and N03 analyses. The above considerations do not take into account the effect of dust on the flow dynamics (e.g., Scoville & Norman 1995; Everett 2003), since none have been detected in NGC 3783. We conclude that radiation pressure force is unlikely to drive the flow in NGC 3783 to the observed velocities.

We note that HIG flows may not be steady state phenomena. In this case, the HIG may have been accelerated in the past (when  $M$  was larger or the object brighter) and we observe it now at its coasting or even decelerating phase. Although plausible (e.g., Chelouche & Netzer 2001), such a model adds little to our understanding of the general phenomenon.

#### 3.2. Thermal Pressure–driven Flows

Acceleration by thermal pressure gradients (see Parker 1958) has been suggested to drive extremely ionized high-temperature gas in AGNs (e.g., Begelman et al. 1983; Krolik & Begelman 1986; Balsara & Krolik 1993; Woods et al. 1996). In particular, Balsara & Krolik (1993) and Woods et al. (1996) presented the results of detailed, time-dependent hydrodynamic calculations of thermal pressure–driven flows for a wide range of initial conditions. The conclusion is that highly ionized gas near its Compton temperature may be driven to terminal velocities of

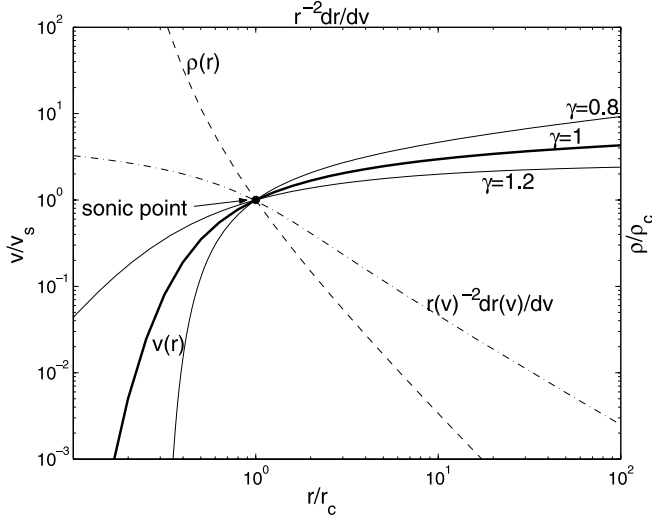


FIG. 2.—Normalized velocity profiles of thermal pressure-driven polytropic flows. Here  $r_c$  is the location of the sonic point (see text). Larger values of  $\gamma$  (i.e., cases in which adiabatic cooling is more important) result in lower velocity for the same sonic point. Also shown is the density profile for a  $\gamma = 1$  isothermal flow (dashed line) that resembles the hydrostatic density profile for  $r < r_c$ . The column density per unit velocity for an isothermal flow at a fixed ionization parameter [ $\propto r(v)^{-2} dr(v)/dv$ ; dash-dotted curve] illustrates the way the opacity decreases with velocity (see § 4.2).

up to  $\sim 2000 \text{ km s}^{-1}$ . Here we investigate the possibility that such a mechanism drives the ionized gas in NGC 3783.

For a spherically expanding flow,

$$\rho \propto r^{-2} v^{-1}. \quad (2)$$

In the limit of  $M \ll \Gamma^{-1}$  (see Fig. 1), assuming a polytropic flow with index  $\gamma$  ( $\gamma = 1$  for isothermal gas), we can rewrite equation (1) as

$$\frac{1}{v} \frac{dv}{dr} = \frac{1}{v^2 - \gamma v_s^2} \left( \frac{2\gamma v_s^2}{r} - \frac{n_e \sigma_T L_{\text{tot}}}{4\pi \rho r^2 c \Gamma} \right). \quad (3)$$

Supersonic steady state winds that are launched subsonically should cross the sonic point at  $r_c = GM_{\text{BH}}/2\gamma v_s^2$ , where  $v(r_c) = \sqrt{\gamma} v_s(r)$ . At this point both the numerator and the denominator vanish; thus, the equation of motion is defined at all radii. Noting that  $M_{\text{BH}} \propto L_{\text{Edd}} \propto L_{\text{tot}}/\Gamma$ , we find

$$r_c \simeq \gamma^{-1} \frac{L_{\text{tot}}}{10^{44} \text{ ergs s}^{-1}} \frac{10^6 \text{ K } 0.1}{T} \frac{1}{\Gamma} \text{ pc}. \quad (4)$$

For a given  $\gamma$ , wind solutions are self-similar and scale with  $v_s$  and  $r_c$ . Several such solutions for different values of  $\gamma$  are shown in Figure 2. The terminal velocity of such flows is on the order of (or a few times larger than) the sound speed at the critical point (i.e., the escape velocity). For isothermal flows, ( $\gamma = 1$ ) the terminal velocity is a few times the sound speed ( $\sim 4v_s$  at  $r \sim 10^2 r_c$ ), while for polytropic flows with  $1 < \gamma < 5/3$ , the terminal velocity is lower because of adiabatic losses (e.g., Lamers & Cassinelli 1999). Polytropic flows for which  $\gamma < 1$  imply excessive heating and result in higher flow velocities.

Also shown in Figure 2 is the density profile for an isothermal flow. For  $r < r_c$  the density profile is similar to that of the hydrostatic case. The density beyond the sonic point declines more

rapidly compared to the hydrostatic case. The column density of the flow, from some value of  $r$  to infinity, is

$$N_{\text{H}}(r) = \int_r^\infty dr' n_{\text{H}}(r'). \quad (5)$$

For supersonic isothermal flows,  $v \propto (\ln r)^{1/2}$  and  $N_{\text{H}} \simeq r n_{\text{H}}(r)$ .

Returning to NGC 3783, we note that the temperature of the high-ionization component found by N03, combined with the mass of the central object in this source, assuming  $\gamma = 1$ , gives (eq. [4])  $r_c \sim 3 \text{ pc}$ . This distance is consistent with the three lower limits on the distance found by N03. Using equation (5) and the density of the hot component found by N03, we get  $N_{\text{H}} \sim 10^{22} \text{ cm}^{-2}$ , which is similar to the column density of this component obtained by N03. Thus, the conditions in this source are consistent with a picture in which the highest ionization gas is in a state of thermal pressure-driven flow. As shown below, there are other observational constraints that are satisfied by such a model.

### 3.3. The Density Structure of the Flow

The continuity condition (eq. [2]) implies  $U_{\text{ox}} \propto v$ . This has been shown to result in high-ionization absorption-line profiles that are more blueshifted and broader compared to low-ionization lines (Chelouche & Netzer 2002). Such trends are not observed in NGC 3783 (Kaspi et al. 2002). In fact, lines of different ionization states are remarkably similar, which indicates similar dynamics. It is unlikely that different ionization components are launched with different initial conditions and end showing the same line profiles. A more likely explanation is that all flow components are cospatial and are accelerated together to their observed velocities (a similar conclusion has been reached by N03 on the basis of the apparent pressure equilibrium between the different phases).

The coexistence of several gas phases is a well-known phenomenon in the interstellar medium (ISM) and in molecular clouds. A multiphase gas naturally occurs for a turbulent medium, where the relation between the density  $\rho$  and the physical scale  $\xi$  follows a power-law distribution,  $\rho \propto \xi^\beta$  (see § 4 for the full definition). Such dependences have been observed on large ( $1-10^3 \text{ pc}$ ; e.g., Elmegreen & Scalo 2004) as well as small ( $10^{15}-10^{18} \text{ cm}$ ; Deshpande 2000) scales.

Consider a small section of the flow over which both  $r$  and  $v$  are constant. Since  $N_{\text{H}}(\xi) \propto \rho \xi \propto \xi^{\beta+1}$  and  $U_{\text{ox}} \propto v$ , we get  $N_{\text{H}} \propto U_{\text{ox}}^\alpha$ , where  $\alpha = -(\beta+1)/\beta$  (cf. Krolik & Kriss 2001). Thus, there is a simple local relationship between the column density and the ionization parameter involving the size distribution parameter of the medium. This dependence holds also for geometrically thick flows and the integrated column density, provided that the self-similar scaling holds for all  $r$  (see § 4.2).

Returning to NGC 3783, we find that the N03 three-component solution implies  $\beta \sim -0.8$ . Such a value of  $\beta$  usually characterizes turbulent media like the ISM and molecular clouds and is consistent with recent simulations (e.g., Boldyrev et al. 2002).

Our model assumes the following range of densities at every location  $r$ :

$$\rho = \rho_{\text{min}} \left( \frac{\xi}{\xi_{\text{max}}} \right)^\beta, \quad (6)$$

where  $\rho_{\text{min}}$  and  $\xi_{\text{max}}$  are the (location dependent) minimum density and maximum length, respectively, and  $\beta$  is a constant to be determined later. We require that the surface of a sphere

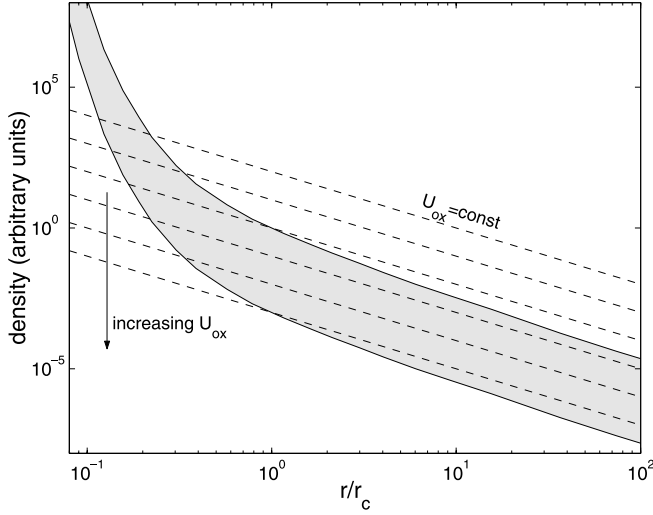


FIG. 3.—Density profile of a multiphase flow with a fixed density contrast. Also shown are lines of constant ionization parameter. Clearly, the expansion of an optically thin (to continuum absorption) flow results in an increase of its mean level of ionization.

with radius  $r$  be fully covered by all phases in the density range  $[\rho_{\min}, \rho_{\max}]$ ,

$$\int d\xi(\rho)^2 = 4\pi r^2. \quad (7)$$

This results in

$$\xi_{\max} = 2\sqrt{\pi}r \left[ 1 - \left( \frac{\rho_{\max}}{\rho_{\min}} \right)^{2/\beta} \right]^{-1/2}, \quad (8)$$

where  $\xi_{\max}$  is defined over the surface of the sphere. Assuming that the density contrast,  $\rho_{\max}/\rho_{\min}$ , is a constant of motion, then  $\xi_{\max} \propto r$ .

The mass-loss rate due to all flow components can be calculated by defining the mean density over a (thin) spherical shell,

$$\langle \rho(r) \rangle = \frac{1}{4\pi r^2} \int d\xi^2 \rho(\xi; r), \quad (9)$$

which can be expressed, using the above relations, as

$$\langle \rho(r) \rangle = \frac{\rho_{\min}}{2\pi(\beta+2)} \left( \frac{\xi_{\max}}{r} \right)^2 \left[ 1 - \left( \frac{\rho_{\max}}{\rho_{\min}} \right)^{(\beta+2)/\beta} \right]. \quad (10)$$

The mass-loss rate is then given by

$$\dot{M} = 4\pi r^2 \langle \rho(r) \rangle v = \frac{8\pi r^2 \rho_{\min} v}{\beta+2} \frac{1 - (\rho_{\max}/\rho_{\min})^{(\beta+2)/\beta}}{1 - (\rho_{\max}/\rho_{\min})^{2/\beta}}. \quad (11)$$

This conforms to the mass-loss rate of a single-phase spherical flow in the limits  $\beta \rightarrow 0$ ,  $\rho_{\max} = \rho_{\min}$ . Assuming a divergence-free flow, mass conservation implies

$$\rho_{\min} r^2 v = \text{const.} \quad (12)$$

This continuity condition is identical in form to that of a single-phase medium. It means that the highest ionization parameter,  $U_{\text{ox}}^{\max}$ , corresponding to the lowest density,  $\rho_{\min}$ , is proportional to the velocity. By construction there are fixed density and

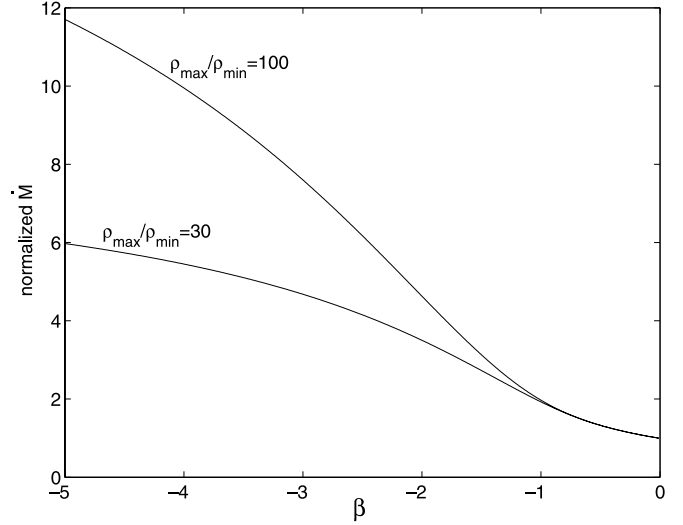


FIG. 4.—Mass-loss rate,  $\dot{M}$ , as a function of the density power-law index  $\beta$  for different values of the density contrast (eq. [11]). Note that  $\dot{M}$  increases with decreasing  $\beta$  and increasing density contrast, since the fraction of the denser regions of the flow is larger in those cases (see text).

ionization parameter contrasts at every location ( $\rho_{\min}/\rho_{\max} = U_{\text{ox}}^{\min}/U_{\text{ox}}^{\max}$ ). An example of a density profile of a multiphase flow is shown in Figure 3, together with several isoionization parameter curves. Clearly, the mean level of ionization increases as the gas expands.

For a given velocity profile, the mass-loss rate depends on the density contrast and  $\beta$ . For a fixed  $\rho_{\min}$ , smaller  $\beta$  and/or larger density contrasts result in denser regions having larger scales and making a larger contribution to  $\dot{M}$ . The differences are small for  $\beta > -1$ , since the mass fraction of the denser regions is negligible (Fig. 4).

The effect of inhomogeneity on the flow dynamics can be approximated by noting that all components in the N03 solution are in a rough pressure equilibrium. Under such conditions one must solve for the combined dynamics of all phases, since their coupling is strong and the momentum is quickly (relative to the dynamical timescale) distributed throughout the flow. The dynamical effect can therefore be included by considering their contribution to the inertial mass. The mean (over volume) density is  $\sim 3/(\beta+3)\rho_{\min}$ . In this approximation, the critical point is given by

$$r_c = [(1 + \beta/3)\gamma]^{-1} \frac{GM_{\text{BH}}}{2v_s^2}, \quad v(r_c) = v_s \sqrt{(1 + \beta/3)\gamma}. \quad (13)$$

In the above analysis we have neglected the effect of drag forces between the different phases. This is justified if such condensations are constantly forming and evaporating on short time-scales compared to the dynamical time and the mean net effect is averaged out. Thus, the flow considered here is very different from other works in which discrete, dynamically independent clouds, rather than time-dependent condensations, are assumed (e.g., Chelouche & Netzer 2001; Everett 2003).

### 3.4. Thermal Balance in a Multiphase Expanding Medium

As demonstrated in several works (e.g., Begelman et al. 1983; Balsara & Krolik 1993; Woods et al. 1996), adiabatic cooling can have an important effect on the thermal equilibrium and, hence, on the dynamics of continuously expanding Compton-heated winds in low-luminosity AGNs. Here we investigate the effect of such cooling on the thermal structure of the multiphased HIG in

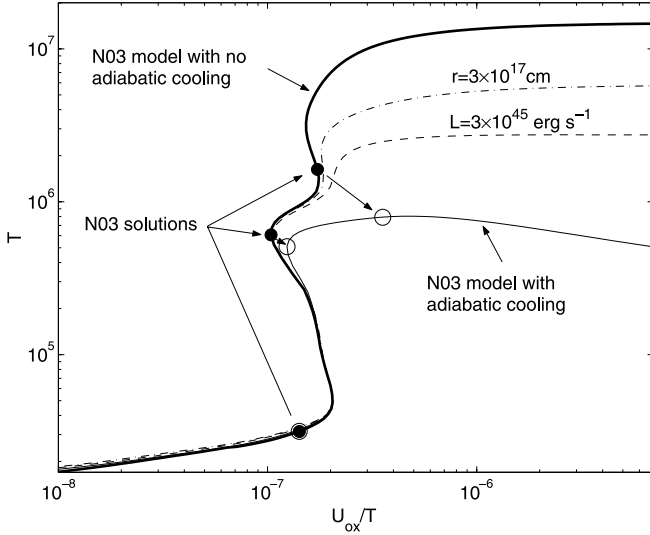


FIG. 5.—Effect of adiabatic cooling on the stability curve of photoionized gas in NGC 3783. In all models the gas is assumed to flow with a velocity of 1000 km s<sup>-1</sup>, the distance is 10<sup>19</sup> cm, and the SED and luminosity ( $3 \times 10^{44}$  ergs s<sup>-1</sup>) are those defined in N03 (see § 2). The thick solid line is the N03 stability curve with their assumed  $r = 10^{19}$  cm and no adiabatic cooling. The thin solid line has the same parameters but includes adiabatic cooling. Additional stability curves that include adiabatic cooling were calculated by varying one parameter at a time,  $r$  or  $L$ . The parameter that was changed is denoted next to the curves.

NGC 3783, where the temperature is below the Compton temperature and the medium may be turbulent.

Neglecting the small contribution due to velocity gradients, the adiabatic cooling term for a spherically expanding continuous flow is

$$\Lambda_{\text{ad}} \simeq 2\rho v_s^2 \frac{v}{r}. \quad (14)$$

The N03 model of NGC 3783 did not include adiabatic cooling. Considering the observed properties of NGC 3783 ( $r = 10^{19}$  cm and  $v \simeq 1000$  km s<sup>-1</sup>) and including the process in the ION thermal calculations, we find that adiabatic cooling lowers the maximum temperature by more than an order of magnitude (see Fig. 5). Since we do not have a numerical hydrodynamic code, we have tested this result against the numerical calculations of Woods et al. (1996) under similar conditions (such as the Eddington ratio, SED, and gas velocity; see their Fig. 14) and find them to be in good agreement. Thus, the numerical approach adopted here gives the correct temperature and expansion velocity required by our calculations. The effect is smaller when the ionizing flux is higher, since heating is proportional to  $L_{\text{tot}}/r^2$  (see the individual curves in Fig. 5). The ionization structure of the flow, and hence  $M$ , are less affected by adiabatic cooling.

Adiabatic cooling also alters the stability curve for the gas. The three N03 solutions still lie on the stable branches of the stability curve, yet the pressure of the high-ionization component is smaller by roughly a factor of 3, so strict pressure equilibrium between all components is not maintained.

The flow considered here is multiphased and turbulent (see § 6.3). In such a case there is an additional internal energy source entrained in the large eddies. This energy is transferred to smaller and smaller scales until it dissipates (e.g., via Coulomb collisions), and it serves as an additional heat source for the gas. The corresponding heating rate is

$$G_{\text{turb}} \simeq \rho \frac{v_{\text{turb}}^3}{r}, \quad (15)$$

where  $v_{\text{turb}}$  is the turbulence velocity (see Bottorff & Ferland 2002). Typically,  $v_{\text{turb}}$  is on the order of  $v_s$  and the flow velocity,  $v$  (e.g., Shu 1992). The size of the largest eddy is comparable to the flow extent and, hence, to  $r$ . Hence, heating by turbulent dissipation can offset the adiabatic cooling. Below, we consider several models in which the two terms play different roles.

#### 4. A THERMAL PRESSURE-DRIVEN FLOW MODEL FOR NGC 3783

In § 3.2 we show a qualitative agreement between the predictions of a multiphase, thermal pressure-driven flow model and the observations of NGC 3783. Section 3.3 outlines the physical model in detail. Here we carry out a more quantitative investigation of the model and apply it to the outflowing gas in NGC 3783. The main aim is to give detailed spectral predictions and compare them to the high-resolution X-ray observations. We use the simplified, steady state treatment of the flow dynamics presented in § 3.2 and a sophisticated scheme for the calculation of the transmitted spectrum through the flow. As explained, the changes in the gas temperature and the attained velocities are in general agreement with more sophisticated hydrodynamic calculations.

Here we assume that the flow evaporates from some mass reservoir (e.g., the accretion disk or the putative torus), expands as it is accelerated to cover a fair fraction of the AGN sky, and crosses our line of sight at some finite radius (to be determined later). Such flow configurations are often assumed in one-dimensional modeling of AGN flows (e.g., Murray et al. 1995) and have been qualitatively confirmed by detailed hydrodynamic simulations of energy-driven flows (e.g., Balsara & Krolik 1993; see also Woods et al. 1996).

##### 4.1. Calculation Scheme

We begin the calculation by specifying the initial conditions. These include the location,  $r_0$ , where the flow enters our line of sight (which need not be equal to  $r_c$ ), and  $U_{\text{ox}}^{\text{max}}(r_0)$  and  $U_{\text{ox}}^{\text{min}}(r_0)$ , which also determine the density contrast throughout the flow. An additional parameter is the density power-law index,  $\beta$ . The other parameters,  $L_{\text{tot}}$  and  $\Gamma$ , are fixed at their observed values.

The next step involves photoionization and thermal calculations of non-LTE gas in statistical equilibrium (this is justified since the dynamical timescales are larger than the recombination timescales by several orders of magnitude; Krolik & Kriss 2001; N03). These calculations are carried out using ION 2004, the 2004 version of the ION photoionization code (e.g., N03, with the addition of new dielectronic recombination rates for iron; see Netzer 2004), which includes all important heating and cooling mechanisms and is suitable for exploring the physics of HIG in photoionization equilibrium. The code includes also the effect of adiabatic cooling on the thermal structure of the highest ionization phase (see eq. [14]). Once the temperature profile of the high-ionization phase is calculated, we approximate it by a polytropic relation ( $T \propto \rho^{\gamma-1}$ ) that provides a good approximation for the cases considered here and solve the equation of motion. (We note that for the relevant parameter space, radiation pressure force acting on the low-ionization phases of the gas has a negligible effect on the global flow dynamics.) The process iterates several times until  $v(r)$  and  $\gamma$  converge.

The next step is to calculate the ionization and thermal structure of all flow phases at location  $r$ . This is done for a flow section of length  $\delta r$  in the radial direction. Here  $\delta r$  is taken as the scale over which the flow velocity changes by 10 km s<sup>-1</sup>. This ensures high-resolution spectral predictions for the absorption

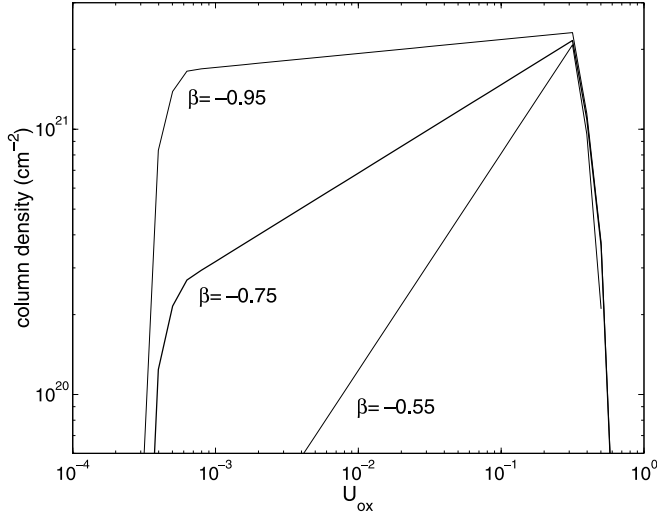


FIG. 6.—Effect of  $\beta$  on the total column density distribution as a function of ionization level (i.e.,  $U_{\text{ox}}$ ). The linear part of the curve is sensitive to  $\beta$  (see text). Steeper density profiles (smaller values of  $\beta$ ) result in the flow being dominated by low-ionization gas.

lines. For this purpose we use a discrete version of the continuous density distribution (eq. [6]) that includes 50 phases corresponding to roughly 0.1 dex intervals in  $U_{\text{ox}}$ . When calculating the transmitted spectrum through sections of the flow, we assume that equation (8) holds also for the line-of-sight direction, albeit with a different normalization (spherical condensations or “clouds” are not the general case under such conditions; e.g., Blumenthal & Mathews 1979). This means that

$$\rho = \rho_{\min} (\xi^l / \xi_{\max}^l)^\beta, \quad (16)$$

where  $\xi^l$  is the length scale in the radial direction and

$$\xi_{\max}^l = \delta r \left[ 1 - \left( \frac{\rho_{\max}}{\rho_{\min}} \right)^{1/\beta} \right]^{-1}. \quad (17)$$

Here  $\xi^l$  is determined by the somewhat arbitrarily defined  $\delta r$  and is therefore independent of  $\xi$ . The ratio  $\xi/\xi^l$  is constant, by construction, for all phases and is their geometric aspect ratio (e.g., Blumenthal & Mathews 1979). This arbitrariness in the shape and the number of condensations (see the Appendix) has no bearing on the results presented in this work that rely on observationally deduced quantities and is related to our ignorance concerning the hydrodynamic properties of such flows and the exact shape (e.g., the number of absorption systems) of the X-ray line profiles.

The contribution of all phases to the line and continuum opacity at each section of the flow is calculated assuming full line-of-sight coverage of the continuum source (see below). The transmitted continuum then serves as the ionizing spectrum for the photoionization calculation of the successive section at  $r + \delta r$ . The velocity shifts at each point are taken into account when calculating the transmitted spectrum. The calculation continues to large  $r$  and produces a high-resolution, theoretical X-ray spectrum.

The global covering fraction of a phase with density  $\rho$  in the range  $[\rho_{\min}(r), \rho_{\max}(r)]$  at a distance  $r$  is given by

$$C(\rho, r) \simeq \frac{\xi(\rho)^2}{4\pi r^2} \frac{\delta r}{\xi^l(\rho)} \sim \left[ \frac{\rho}{\rho_{\min}(r)} \right]^{1/\beta}. \quad (18)$$

Clearly, the covering factor, expressed in this way, can be much smaller than unity for the denser phases and can significantly affect the transmitted continuum through the flow. However, this is only a geometric definition, and the more relevant quantity is the velocity-dependent covering factor,  $C(\rho, v)$ , which takes into account the gas motion and thus enables the proper treatment of the opacity (e.g., Gabel et al. 2003a). We note that, in a turbulent flow, there is no one-to-one correspondence between  $v$  and  $r$ . Turbulence broadens the lines and increases  $C(\rho, v)$  (see also § 5).

#### 4.2. Dependence on Initial Conditions

The solution of the self-consistent model depends on several initial and boundary conditions. The dependence on the initial conditions of the problem,  $\beta$ ,  $U_{\text{ox}}^{\max}$ ,  $U_{\text{ox}}^{\min}$ , and  $r_0$ , is discussed here for the case of isothermal flows. Qualitatively similar results are obtained also for polytropic flows.

We first explore the dependence of the column density distribution on  $U_{\text{ox}}$  and  $\beta$ . As discussed in § 3.3 and shown in Figure 6,  $\beta$  affects the column density distribution such that smaller  $\beta$  results in larger columns of low-ionization gas. The expansion of the flow and the imposed boundary conditions result in rapid decline of the column density for extreme values of  $U_{\text{ox}}$ . Different column densities result in different transmitted spectra. This is shown in Figure 7, where we find that smaller  $\beta$  result in more opaque flows. The effect can be dramatic even for a change of 0.2 in  $\beta$  in cases of large integrated columns. Smaller density contrasts, i.e., larger  $U_{\text{ox}}^{\min}$  at a fixed  $U_{\text{ox}}^{\max}$ , result in smaller columns of less ionized gas (Fig. 6) and therefore lower opacity and higher transmitted soft X-ray flux (i.e., softer spectra; Fig. 7).

The distance,  $r_0$ , at which the flow crosses our line of sight with velocity  $v_0$ , affects the total column density of the flow. The effect is manifested as a change in the X-ray “color.” For example, smaller  $r_0$  values imply larger densities, more opaque gas, and harder X-ray spectra. This is especially important if our line of sight crosses the subsonic section of the flow ( $r_0 < r_c$ ), given the nearly hydrostatic structure of the gas.

We next consider the effect of initial conditions on the absorption-line profiles and assume, for demonstrative purposes, that lines are produced throughout the flow by a single ionization

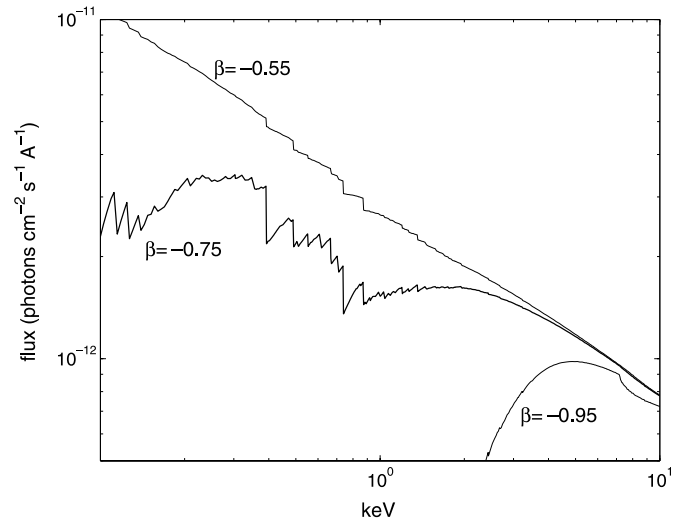


FIG. 7.—Effect of  $\beta$  on the transmitted spectrum. Steeper density profiles (smaller values of  $\beta$ ) result in low-ionization gas contributing more to the gas opacity, with a stronger suppression of the soft X-ray flux.

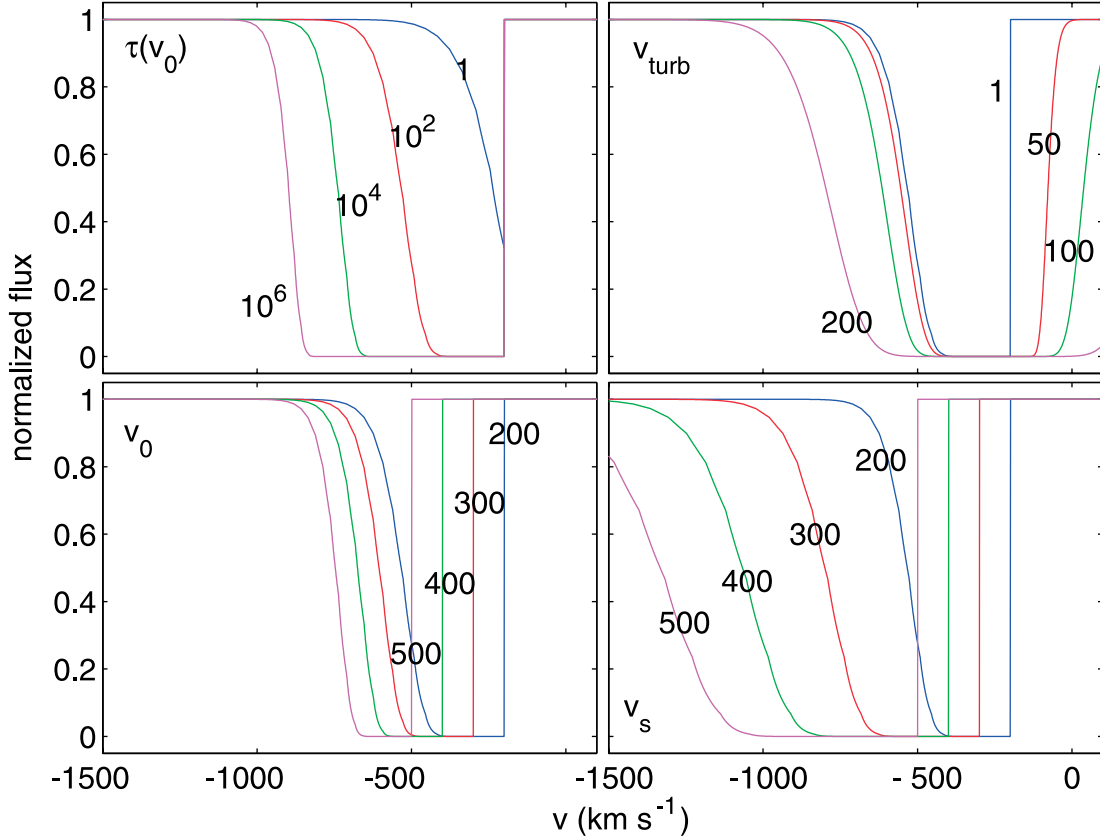


FIG. 8.—Absorption-line profiles as a function of  $\tau(v_0)$  (top left),  $v_{\text{turb}}$  (top right),  $v_0$  (bottom left), and  $v_s$  (bottom right; here  $v_0 = v_s$  is assumed). The model marked by a blue line in all panels corresponds to  $\tau(v_0) = 10^2$ ,  $v_{\text{turb}} = 1$ ,  $v_0 = 200 \text{ km s}^{-1}$ , and  $v_s = 200 \text{ km s}^{-1}$ . All line profiles exhibit an extended blue wing.

phase (i.e., over a narrow range in  $U_{\text{ox}}$ ). In such a case, the optical depth as a function of velocity (for a phase with a given  $U_{\text{ox}}$ ) is

$$\tau(v) \propto \int_0^\infty dv' r(v')^{-2} \frac{dr(v')}{dv'} \exp\left(\frac{v - v'}{2v_{\text{turb}}^2}\right), \quad (19)$$

where we have assumed a Gaussian kernel for line broadening due to, e.g., a turbulent velocity field. The dependence of the line profile on  $\tau(v_0)$  (the optical depth at  $v_0$ ),  $v_{\text{turb}}$ , and  $v_s$  is shown in Figure 8. The calculations show that all line profiles exhibit extended blue wings due to the flow expansion, with the most extreme line asymmetries occurring for optically thin lines [e.g.,  $\tau(v_0) \sim 1$ ]. Larger values of  $v_{\text{turb}}$  broaden the lines and make them more symmetrical with respect to  $v_0$ . The value of  $v_0$  naturally causes a line shift such that larger  $v_0$  result in more blueshifted, narrower lines for the same  $v(r)$ . When calculating the effect of the sound speed (of the highest ionization component),  $v_s$ , on the line profile, we have assumed  $v_0 = v_s$ , which is relevant to supersonic flows that are optically thin in the continuum. As shown, larger values of  $v_s$  imply larger terminal velocities and considerably broader lines. Obviously, the observed line profiles may have a more symmetrical shape depending on the spectral resolution of the instrument.

### 5. FITTING THE 900 ks *CHANDRA* SPECTRUM OF NGC 3783

We resort to an iterative scheme to fit the observed high-resolution X-ray spectrum of NGC 3783. We first try to constrain the flow dynamics. This is accomplished by taking the

theoretical line profiles, normalizing the column densities to agree with those obtained by N03, and convolving the calculated profile with the known instrumental profile (Kaspi et al. 2002). A comparison between the predicted and the observed line profiles defines a narrow range of values of  $r_c$  (and, hence,  $v_s$  and conversely  $U_{\text{ox}}^{\text{max}}$ ),  $v_0$ , and  $v_{\text{turb}}$ . An initial estimate for  $\beta$

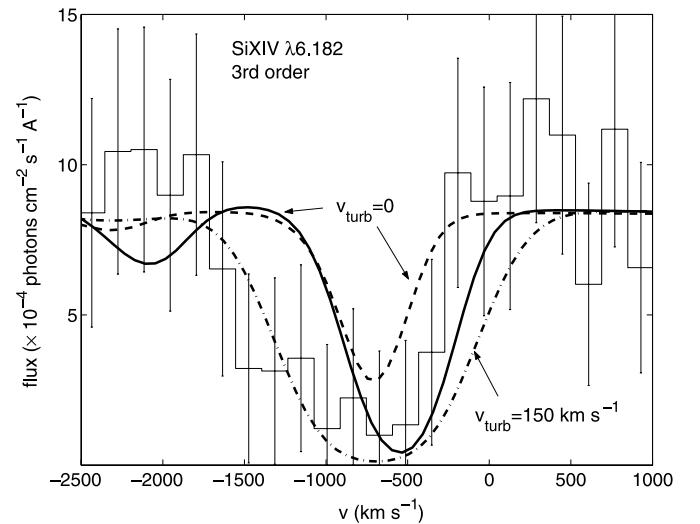


FIG. 9.—Comparison of the calculated Si xiv  $\lambda 6.182$  line profile with the third-order Medium Energy Grating (MEG) data of NGC 3783. The solid line shows an adiabatic model that crosses our line of sight at its sonic point at 0.5 pc. Such a model cannot account for the observed blueshift or width of the line. A nonturbulent flow that crosses our line of sight at 1.5 pc has a more blueshifted centroid but a small equivalent width (dashed line). A similar but turbulent ( $v_{\text{turb}} = 150 \text{ km s}^{-1}$ ) flow provides a better fit to the data (dash-dotted line).

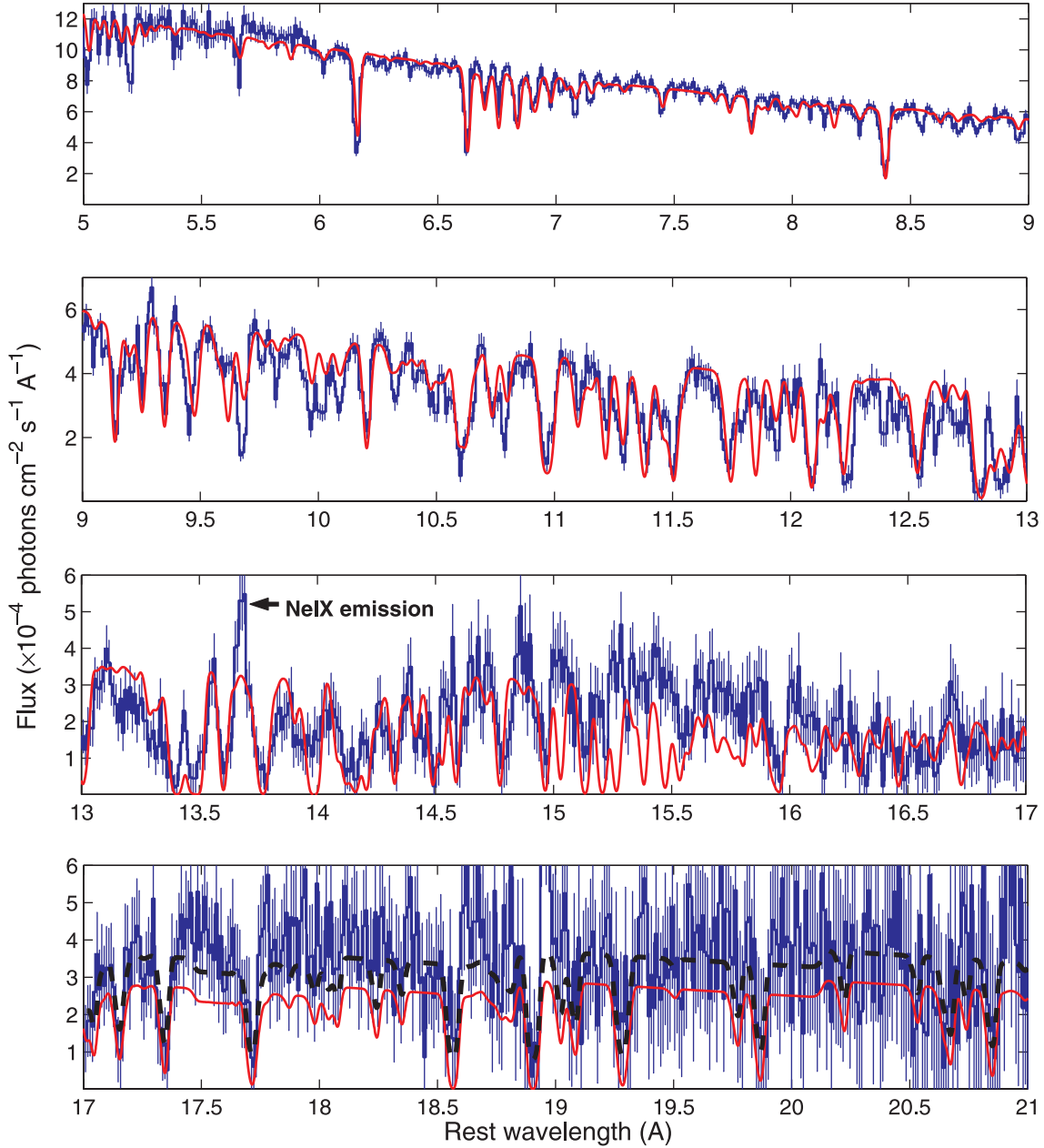


FIG. 10.—Full fit to the 900 ks *Chandra* HETG X-ray spectrum of NGC 3783. This is a pure absorption model, and line and continuum emission is not included. The model provides an acceptable fit over most bands but does not reproduce well the shape of the unresolved transition array near 15–16 Å. The solid line assumes full line-of-sight coverage of the source, and the dashed line in the bottom panel assumes an 80% coverage. The mismatch near 5.5 Å is due to a well-known calibration effect (N03).

comes from the scaling of the column density with ionization parameter (see § 3.3). This allows us to employ the next step in our fitting scheme, which is a more systematic and time-consuming search in a localized region of the parameter space, involving complex spectral calculations (§ 4.2).

The calculated line and continuum spectra take into account the probability of our line of sight intersecting any given phase at every location in the flow (see § 4.2). We assume that the finite thermal and turbulent broadening results in  $C(\rho, v) = 1$  (the opacity at every velocity bin is properly scaled so that the integrated column density is conserved). The best-fit model is obtained by comparing the detailed theoretical spectrum to the observed spectral shape and to individual absorption-line profiles. All calculations assume a photon continuum slope,  $\Gamma = 1.6$ , which best characterizes the hard X-ray spectrum of this source.

Considering only radiative heating and cooling and adiabatic cooling, we find a set of models (hereafter adiabatic models) that are consistent with the spectral shape and whose critical point is about 0.5 pc from the center, with  $r_0 = r_c$ . The density contrast of the flows spans more than 4 orders of magnitude at every location (e.g.,  $U_{\text{ox}}^{\text{min}} \sim 10^{-4}$  and  $U_{\text{ox}}^{\text{max}} \simeq 0.4$  at  $r_0 \sim 1$  pc). Such flows reach a velocity of about 600 km s<sup>-1</sup>, and the absorption-line profiles, convolved with the instrumental resolution, are shown in Figure 9. Clearly, the predicted lines are narrower and less blueshifted than those observed. A better fit is obtained by requiring that the flow cross our line of sight at a large distance ( $\sim 1.5$  pc) and that the line profiles are broadened by a turbulent velocity field. For Si xiv  $\lambda 6.182$ , a  $v_{\text{turb}} \sim 150$  km s<sup>-1</sup> provides a better fit to the data (Fig. 9).

The observational indication for the existence of turbulence suggests that the thermal equilibrium of the gas may be affected



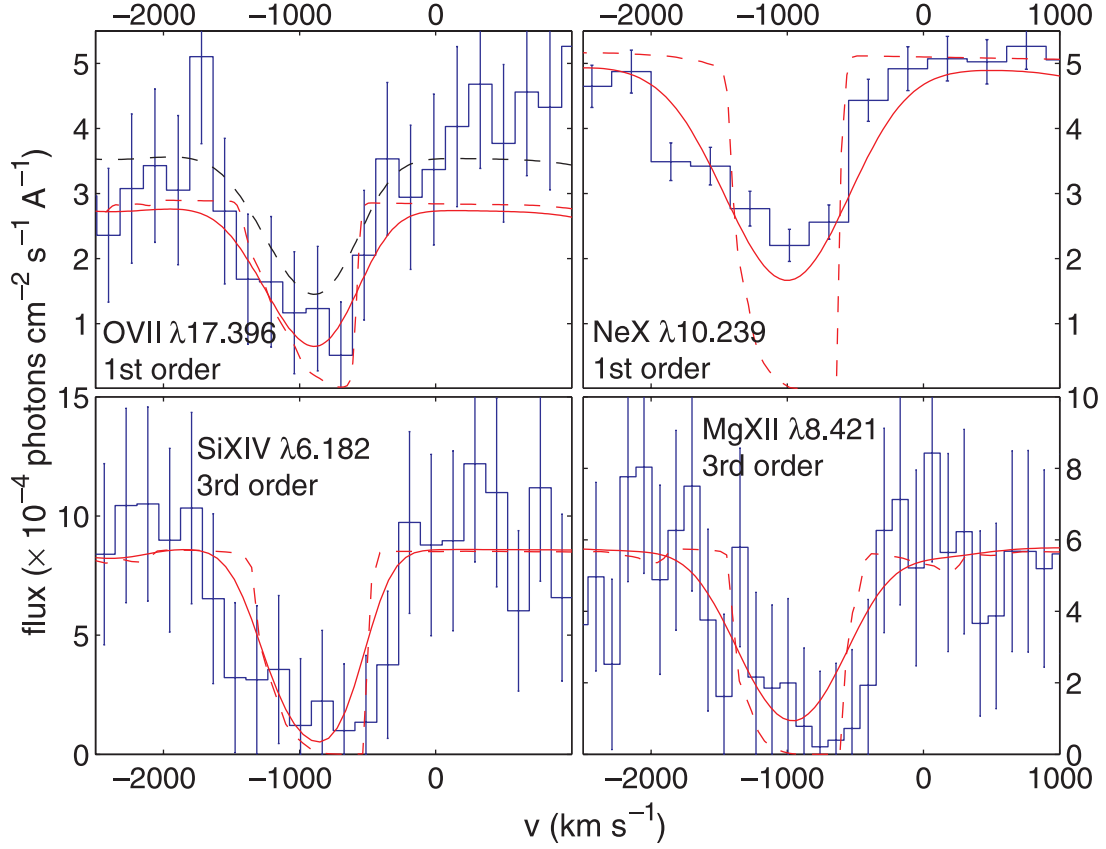


FIG. 11.—Best-fit model to the MEG and High Energy Grating first- and the MEG third-order absorption-line profiles (model parameters are given in Table 2). The spectral model (*solid line*) was convolved with the instrumental resolution relevant to each case. Note the clear blue asymmetry of all predicted, nonconvolved line profiles (*dashed red lines*).

by it. Because of the uncertainties associated with the combined effects of adiabatic cooling and turbulent dissipation heating, we study a case in which  $\Lambda_{\text{ad}} = G_{\text{turb}}$  and radiative processes are the only important heating and cooling mechanisms. In this case, the high-ionization, volume filling phase of the flow may be considered isothermal (e.g., Begelman et al. 1983). We refer to it as the isothermal model but note that all components that are not fully ionized have radial temperature dependence.

The best-fit isothermal model is shown in Figure 10 (a similar fit is obtained for models using either of the full line-of-sight coverage methods described in § 4.2). Clearly, the model is acceptable and is qualitatively similar to the best-fit model of N03. Inspection of individual absorption-line profiles (Fig. 11) shows qualitative agreement with respect to the line centroids

and widths. The derived mass-loss rate is  $\dot{M} \sim 10^{-0.8 \pm 0.6} C M_{\odot} \text{ yr}^{-1}$  (for  $C \simeq 0.2$  [N03],  $\dot{M} \sim 0.01\text{--}0.1 M_{\odot} \text{ yr}^{-1}$ ), i.e., considerably smaller than the N03 and the Behar et al. (2003) estimates. The model also gives detailed predictions for the column densities of various ions. These are given in Table 1 for the more abundant elements. Clearly, the stratified structure of the flow results in a wide range of ionization levels having comparable column densities. We discuss the implications of these results in § 6.2.

The range of parameters characterizing acceptable models are given in Table 2. The quoted uncertainties refer to differences between the adiabatic and isothermal models, the mass of the central object, and the degeneracy in the spectral fit. Specifically, the error in the value of each parameter represents the

TABLE 1  
ION COLUMN DENSITIES

Element	I	II	III	IV	V	VI	VII	VIII	IX	X	XI	XII	XIII	XIV
H.....	16.5	...	...	...	...	...	...	...	...	...	...	...	...	...
He.....	13.7	19.3	...	...	...	...	...	...	...	...	...	...	...	...
C.....	7.4	12.2	15.3	16.6	17.8	18.0	...	...	...	...	...	...	...	...
N.....	6.5	11.5	14.9	16.5	16.8	17.4	17.5	...	...	...	...	...	...	...
O.....	6.8	11.9	15.5	17.0	17.4	17.5	18.1	18.2*	...	...	...	...	...	...
Ne.....	6.0	11.3	14.8	16.2	17.0	17.2	16.8	16.8	17.4	17.6	...	...	...	...
Mg.....	7.8	10.4	13.6	14.7	15.3	16.1	16.4	16.6	16.7	16.7	17.1*	17.2*	...	...
Si.....	6.5	10.2	12.2	13.4	14.9	15.8	16.2	16.5	16.6	16.7	16.7*	16.6*	17.1*	17.2*

NOTES.—Column densities of various ions for our best-fit model, given in  $\log(\text{cm}^{-2})$ . The asterisks (\*) mark deviations of more than a factor of 2 from those deduced from observations and reported by N03.

TABLE 2  
BEST-FIT MODEL PARAMETERS

Parameter	Value
Critical distance $r_c$ ( $10^{18}$ cm) .....	$2.0 \pm 1.5$
Line-of-sight crossing distance $r_0$ ( $10^{18}$ cm).....	$5 \pm 2$
Maximum ionization parameter at $r_0$ [ $\log(U_{\text{ox}}^{\text{max}})$ ] .....	$0.5 \pm 0.3$
Minimum ionization parameter at $r_0$ [ $\log(U_{\text{ox}}^{\text{min}})$ ] .....	$-3.7 \pm 1.5$
Density spectrum index ( $\beta$ ) .....	$-1.2 \pm 0.5$
Mass-loss rate ( $M_{\odot} \text{ yr}^{-1}$ ).....	$10^{-0.8 \pm 0.6} C^a$

<sup>a</sup> For  $C \sim 0.2$  (N03),  $\dot{M}$  is in the range  $0.01\text{--}0.1 M_{\odot} \text{ yr}^{-1}$ .

maximum deviation from the best-fit value for which a good fit can be obtained by varying all the other parameters in the table. Thus, uncertainties in different parameters are not independent.

## 6. DISCUSSION

We have introduced a new approach for modeling highly ionized flows in AGNs. The emerging physical picture for the X-ray flow in NGC 3783 is that of a multiphased, geometrically thick flow that is thermally evaporated from a parsec-scale region. The density range ( $\sim 10^2\text{--}10^6 \text{ cm}^{-3}$  at  $r_0$ ) occupied by the flow is much larger than that obtained by Krongold et al. (2003) and N03, and it implies a density of the warm absorbing phase that is, on average, lower than that suggested by Reynolds & Fabian (1995) and Bottorff & Ferland (2001). Our model has extremely ionized dynamical components that are not detected spectroscopically. The least ionized components are also absent in previous works, since it is difficult to disentangle the ionization level–column density degeneracy.

### 6.1. Is the Flow Turbulent?

The above analysis suggests that the outflowing HIG is turbulent for several reasons: (1) The flow is multiphased with different phases at a rough pressure equilibrium. (2) The density spectrum (i.e.,  $\beta$ ) is similar to that found in the ISM and in molecular clouds, which are known to be turbulent media. (3) The Reynolds number of the flow is  $\text{Re} \sim 10^7$ . This is obtained by assuming nonmagnetic plasma and taking the scale of the largest eddies to be  $r_0$ , the velocity to be  $v_c$ , and the density to be that of the highest ionization phase (see, e.g., eqs. [3.25] and [3.30] in Lang 1999). Such a medium is capable of sustaining turbulent motion. The density or range in our model spans roughly 5 orders of magnitude (corresponding to  $U_{\text{ox}}^{\text{max}}/U_{\text{ox}}^{\text{min}}$ ). This agrees with the naive theoretical expectation that the maximum density is that at which the energy cascade is terminated and the energy is dissipated. This occurs when the density range spans roughly  $\sim 3 \log(\text{Re})/4 \simeq 5 \text{ dex}$  (e.g., Shu 1992). This is consistent with the results obtained from the spectral fit.

Our model does not explain the onset of turbulence in the flow. One possibility is that it is triggered by the putative central star cluster within the central parsec of NGC 3783.

### 6.2. The UV–X-Ray Connection

Table 2 suggests that the X-ray flow in NGC 3783 may also produce strong low-ionization UV absorption lines of H I  $\lambda 1216$ , C IV  $\lambda 1548$ , and O VI  $\lambda 1035$ . Our predictions are consistent with the lower limit on the column density of C IV deduced by Crenshaw et al. (1999). The model suggests that the global covering factor is smaller for lower ionization gas phases

(eq. [18]). This and the fact that the UV continuum–emitting source is likely to be larger than the X-ray source imply that the UV line profiles may be prone to partial line-of-sight coverage effects. This may be manifested either as multicomponent absorption (i.e., not all flow phases are represented in every velocity bin; see § 4.2) or as nonblack saturation (e.g., Gabel et al. 2003a). The current resolution of the X-ray gratings and the signal-to-noise level of the observation are not high enough to tell which of these scenarios is relevant to NGC 3783.

The dynamical timescale of the flow,  $r_0/v_s$ , is about  $10^4 \text{ yr}$ . Gabel et al. (2003b) reported a considerable velocity shift ( $\sim 50 \text{ km s}^{-1}$ ) of the highest velocity component over less than a year. Clearly, the two timescales do not agree. It is, however, possible that a filament moving across our line of sight rather than a real deceleration of the flow is responsible for the observed effect (see also Gabel et al. 2003b). The relevant timescale in this case is the time it takes a filament to cross the surface of the UV-emitting region. Assuming this region to be on the order of  $10R_s$ , where  $R_s$  is the Schwarzschild radius ( $\sim 10^{13} \text{ cm}$  in the case of NGC 3783) and the velocity across the line of sight to be on the order of the thermal speed, we get a crossing timescale of  $\sim 0.3 \text{ yr}$ , i.e., consistent with observations. We conclude that either the high-velocity decelerating UV component is not related to the X-ray flow or else the apparent deceleration is caused by line-of-sight effects.

### 6.3. Extended Emission

Some Seyfert 1 galaxies show evidence of extended, diffuse X-ray emission (e.g., NGC 3516; George et al. 2002). This is also common in Seyfert 2 galaxies. A natural question is whether the extended HIG flow is partly responsible for such emission through the scattering of continuum photons into our line of sight. The expected scattered X-ray luminosity, assuming pure electron scattering, is

$$L_{\text{scat}}^{\text{X}} \simeq \tau_e C L_{\text{tot}}^{\text{X}}, \quad (20)$$

where  $\tau_e$  is the Compton optical depth and  $L_{\text{tot}}^{\text{X}}$  is the total X-ray luminosity. It is possible to relate  $\tau_e C$  to the total mass-loss rate of the flow,  $\dot{M}$ , via

$$\tau_e C = \frac{\sigma_T \dot{M}}{4\pi m_{\text{H}}} \int_{r_e}^{\infty} r^{-2} v^{-1} dr, \quad (21)$$

where  $r_e$  is the distance beyond which  $L_{\text{scat}}^{\text{X}}$  is calculated. This gives

$$\frac{L_{\text{scat}}^{\text{X}}}{L_{\text{tot}}^{\text{X}}} \simeq (6 \times 10^{-6}) \frac{\dot{M}}{1 M_{\odot} \text{ yr}^{-1}} \frac{1 \text{ kpc}}{r_e} \frac{10^3 \text{ km s}^{-1}}{v}. \quad (22)$$

The extended ( $r_e \sim 0.5 \text{ kpc}$ ) X-ray flux from NGC 3783 is  $< 10^{36} \text{ ergs s}^{-1}$  (I. George 2004, private communication), i.e., consistent with model predictions (see Table 1).

### 6.4. Relation to Other AGN Components

So far, we have not considered the source of the outflowing gas. Our model suggests that, for NGC 3783, it is located within the central  $\sim 1 \text{ pc}$ . A possible mass reservoir on such scales is the putative molecular torus (e.g., Krolik & Begelman 1988; Krolik & Kriss 1995; Netzer et al. 2002). Taking the torus

parameters from Netzer et al. (2002), we obtain that the torus mass is  $\sim 10^5 M_\odot$  and that HIG flows may be sustained at their current mass-loss rates for  $\sim 10^6$ – $10^8$  yr. If, as suggested by Krolik & Begelman (1988), the torus is also responsible for feeding the AGN, then this timescale also corresponds to the present activity lifetime.

The narrow-line region (NLR) lies at the outskirts of the HIG flow and hence is exposed to a modified type I AGN continuum. Similar conclusions (albeit with somewhat more diminished UV fluxes compared to the model presented here) have been reached by Alexander et al. (1999) on the basis of the analysis of narrow emission lines in NGC 4151. A physical interaction between the HIG outflow and the NLR is unlikely to be energetically important, given the small mass-loss rate derived here (e.g., Laor 1998).

### 6.5. Model Limitations and Extensions

Despite the success of our model in explaining the observed X-ray features, there are several notable problems.

#### 6.5.1. Flow Dynamics

In its simplest form (without turbulent line broadening or dissipative heating) our model underpredicted the line widths and blueshifts. One possibility, discussed in §§ 5 and 6.1, is that the flow is turbulent. Alternatively, higher flow velocities and better agreement with the data may be obtained if the flow is launched closer in to the central source. This requires, however, that the mass of the central object be smaller by a factor of a few compared to that reported in Peterson et al. (2004; see also § 6.5.2). Another possibility is that the flow dynamics reflects a higher mean past luminosity compared with the one deduced from the present observations. In both cases, adiabatic cooling is less important (see § 3.4) and radiative acceleration is more effective (since  $\Gamma$  is larger). Our calculations show that in such cases the terminal velocity is slightly larger (by  $\sim 300$  km s $^{-1}$ ) than that of the isothermal model (see § 5) and the fit is qualitatively similar.

#### 6.5.2. Flow Location

The value of  $r_0$  derived here is smaller than the lower limit derived by N03 on the distance of the multiphased flow but is larger than the upper limit for the highest ionization component by itself. Nevertheless, the model is consistent with the lack of appreciable equivalent width (EW) variations of the silicon and sulfur lines, since the multiphase flow is geometrically thick. Note also that  $r_c$  and  $r_0$  depend linearly on the mass of the central object, which is somewhat uncertain. For example, Kaspi et al. (2000b) report  $M_{\text{BH}} \sim 10^7 M_\odot$ , i.e., a factor of 3 lower than the new Peterson et al. (2004) estimate. A model having similar spectral properties would have  $r_c \sim 0.13$  pc and  $r_0 \sim 0.5$  pc (compared with the present  $r_c = 2$  pc and  $r_0 = 5$  pc) for such low values of  $M_{\text{BH}}$  (eq. [4]).

Reeves et al. (2004) reported *XMM-Newton* EPIC pn observations showing significant EW variations of Fe xxiii and Fe xxiv absorption lines near 2 Å. The lines are consistent with the highest ionization N03 model yet according to Reeves et al.; they suggest the gas lies within the central 0.02 pc. We have checked this suggestion within the general N03 model. Assuming that the reported line variability is real and using the mean N03 continuum luminosity, we find that the photoionization timescale of Fe xxiii gives an upper limit of  $\sim 0.2$  pc, basically identical to the value denoted in N03. This value of  $r_0$  is,

however, inconsistent with the lower limits on the location of the two more neutral, higher density components. Thus, the Reeves et al. (2004) observation presents a real difficulty to our multiphase model in which all components are present at all locations. It remains to be seen whether the high-ionization gas component reported by Reeves et al. is part of the outflow in NGC 3783.

#### 6.5.3. Thermal Instability

Our model assumes a continuous range of densities and therefore ionization levels and temperatures. However, some phases of our model lie on thermally unstable branches of the stability curve (see Fig. 5). In this case the gas may undergo nonlinear compression or expansion following some initial perturbation and end up in a thermally stable equilibrium. This effectively changes the assumed  $\rho$ - $\xi$  distribution. The appropriate modeling of such conditions is beyond the scope of this paper.

#### 6.5.4. Spectral Deviations

Our model predicts lower flux levels than those observed at soft X-ray energies. This discrepancy is eliminated if one takes into account partial covering (N03). Such an effect is, in fact, expected since the low-ionization gas is likely to have lower global coverage. A continuum leakage of 20% (80% flow coverage) improves our fit and correctly predicts the depth of the (saturated but nonblack) O viii lines. Another discrepancy is evident near 15–16 Å, where our model predicts too much absorption by highly ionized iron lines. This may be related to the dielectronic recombination rates of some of these ions (e.g., Netzer 2004). Also, Figure 10 does not include emission features from the flow, which results in underprediction of the flux in several bands (e.g., near the Ly $\alpha$  line of Ne ix at 13.6 Å; see Kaspi et al. 2002).

Kaspi et al. (2002) showed that some X-ray line profiles exhibit two absorption components. Our model assumes a smooth flow and, therefore, smooth line profiles. Multicomponent absorption can be accounted for in two ways: (1) It is possible that the high-velocity component seen in Kaspi et al. (2002) is due to a flow that is launched closer in to the central source, where the temperature of the highest ionization component is higher and the escape velocity is larger. (2) Absorption may be deficient at some intermediate velocities (e.g., due to a “missing” phase at some location; see § 6.2). Modeling such multivelocity flows is beyond the scope of this paper.

## 7. SUMMARY

We presented a novel method for modeling the properties of highly ionized flows in AGNs. We performed state-of-the-art photoionization, dynamical, and spectral calculations and compared our results to the 900 ks *Chandra* HETG spectrum of NGC 3783. The model is consistent with several independent observational constraints including the continuum and line spectrum, spectral variations (or the lack of), and the upper limit on extended emission from this source. Our major conclusions can be summarized as follows: (1) The flow in this source is geometrically thick and is driven primarily by thermal pressure gradients. (2) The flow is multiphased, with a density-size spectrum that resembles that of a turbulent medium. Adiabatic cooling and turbulent heating are likely to be important in the energy balance. (3) The gas is located beyond the BLR and within the NLR. Its origin may be related to the putative torus. (4) The mass-loss rate is on the order of the mass accretion rate in this object, and the kinetic luminosity is very small ( $< 0.1\%$ ) compared

to the bolometric luminosity of the source. (5) The same flow may also account for some of the UV lines observed in this source.

We thank Shai Kaspi for invaluable help in dealing with the complex *Chandra* spectrum of NGC 3783. We thank N. Murray

and J. Everett for fruitful discussions. The referee is thanked for his or her very constructive comments. While at Tel Aviv University, D. C. was partly supported by the Dan David Prize Foundation through the Dan David Prize scholarship. This research has been supported by Israel Science Foundation grant 232/03 and by NASA through Chandra Postdoctoral Fellowship award PF4-50033.

## APPENDIX

### ALTERNATIVE DERIVATION OF THE FLOW EQUATIONS

It is possible to derive the flow equations using the volume filling factor formalism adopted by Arav et al. (1994) in their modeling of outflowing broad absorption-line regions. The Arav et al. model assumes confined clouds and may not be suitable for describing the highly ionized gas condensations considered here. Nevertheless, a comparison between the two approaches is useful.

Define a volume filling factor by

$$\epsilon(\rho) = \epsilon_{\max} \left( \frac{\rho}{\rho_{\min}} \right)^{\eta}. \quad (\text{A1})$$

We require that all flow phases fill the entire available volume, i.e.,  $\int d\epsilon = 1$ , to obtain

$$\epsilon_{\max} = \left[ 1 - \left( \frac{\rho_{\max}}{\rho_{\min}} \right)^{\eta} \right]^{-1}. \quad (\text{A2})$$

For a divergence-free spherically expanding flow,

$$\dot{M} = 4\pi r^2 v \int_{\rho_{\min}}^{\rho_{\max}} d\rho \epsilon(\rho) = \frac{4\pi r^2 \rho_{\min} v}{\eta + 1} \frac{1 - (\rho_{\max}/\rho_{\min})^{\eta+1}}{1 - (\rho_{\max}/\rho_{\min})^{\eta}} = \text{const}, \quad (\text{A3})$$

which, for a flow with a fixed density contrast, results in

$$\rho_{\min} r^2 v = \text{const}. \quad (\text{A4})$$

This is identical to equation (12) and suggests that the continuity condition is not because of our choice of formalism.

Consider now a volume  $V$  filled with a number of different density phases, where a phase of density  $\rho$  occupies  $\epsilon(\rho)$  of the volume. If that phase is composed of  $n$  identical spherical clouds, then the volume of each cloud is  $n^{-1}\epsilon(\rho)V$ . The total surface covered by such clouds is  $\simeq n(n^{-1}\epsilon V)^{2/3} = n^{1/3}(\epsilon V)^{2/3}$ . Thus, the global  $(4\pi)$  covering factor due to this phase is  $C_g(\rho) \propto n^{1/3}\epsilon(\rho)^{2/3}$ .

## REFERENCES

- Alexander, T., Sturm, E., Lutz, D., Sternberg, A., Netzer, H., & Genzel, R. 1999, *ApJ*, 512, 204  
 Arav, N., Li, Z., & Begelman, M. C. 1994, *ApJ*, 432, 62  
 Balsara, D. S., & Krolik, J. H. 1993, *ApJ*, 402, 109  
 Begelman, M. C., McKee, C. F., & Shields, G. A. 1983, *ApJ*, 271, 70  
 Behar, E., Rasmussen, A. P., Blustin, A. J., Sako, M., Kahn, S. M., Kaastra, J. S., Branduardi-Raymont, G., & Steenbrugge, K. C. 2003, *ApJ*, 598, 232  
 Blumenthal, G. R., & Mathews, W. G. 1979, *ApJ*, 233, 479  
 Boldyrev, S., Nordlund, Å., & Padoan, P. 2002, *Phys. Rev. Lett.*, 89, 031102  
 Bottorff, M., & Ferland, G. 2001, *ApJ*, 549, 118  
 ———. 2002, *ApJ*, 568, 581  
 Bottorff, M. C., Korista, K. T., & Shlosman, I. 2000, *ApJ*, 537, 134  
 Branduardi-Raymont, G., Sako, M., Kahn, S. M., Brinkman, A. C., Kaastra, J. S., & Page, M. J. 2001, *A&A*, 365, L140  
 Chartas, G., Brandt, W. N., Gallagher, S. C., & Garmire, G. P. 2002, *ApJ*, 579, 169  
 Chelouche, D., & Netzer, H. 2001, *MNRAS*, 326, 916  
 ———. 2002, in *ASP Conf. Ser. 255, Mass Outflow in Active Galactic Nuclei: New Perspectives*, ed. D. M. Crenshaw, S. B. Kraemer, & I. M. George (San Francisco: ASP), 315  
 ———. 2003a, *MNRAS*, 344, 223  
 ———. 2003b, *MNRAS*, 344, 233  
 Crenshaw, D. M., Kraemer, S. B., Boggess, A., Maran, S. P., Mushotzky, R. F., & Wu, C. 1999, *ApJ*, 516, 750  
 Deshpande, A. 2000, *MNRAS*, 317, 199  
 Elmegreen, B. G., & Scalo, J. 2004, *ARA&A*, 42, 211  
 Everett, J. 2003, Ph.D. thesis (Univ. Chicago)  
 Gabel, J. R., et al. 2003a, *ApJ*, 583, 178  
 Gabel, J. R., et al. 2003b, *ApJ*, 595, 120  
 George, I. M., Turner, T. J., Netzer, H., Nandra, K., Mushotzky, R. F., & Yaqoob, T. 1998, *ApJS*, 114, 73  
 George, I. M., Turner, T. J., Yaqoob, T., Netzer, H., Laor, A., Mushotzky, R. F., Nandra, K., & Takahashi, T. 2000, *ApJ*, 531, 52  
 George, I. M., et al. 2002, *ApJ*, 571, 265  
 Halpern, J. P. 1984, *ApJ*, 281, 90  
 Hamann, E., & Ferland, G. 1993, *ApJ*, 418, 11  
 Kaastra, J. S., Mewe, R., Liedahl, D. A., Komossa, S., & Brinkman, A. C. 2000, *A&A*, 354, L83  
 Kaspi, S., Brandt, W. N., Netzer, H., Sambruna, R., Chartas, G., Garmire, G. P., & Nousek, J. A. 2000a, *ApJ*, 535, L17  
 Kaspi, S., Smith, P. S., Netzer, H., Maoz, D., Jannuzi, B. T., & Givon, U. 2000b, *ApJ*, 533, 631  
 Kaspi, S., et al. 2001, *ApJ*, 554, 216  
 ———. 2002, *ApJ*, 574, 643  
 King, A. 2003, *ApJ*, 596, L27  
 Königl, A., & Kartje, J. F. 1994, *ApJ*, 434, 446  
 Krolik, J. H., & Begelman, M. C. 1986, *ApJ*, 308, L55  
 ———. 1988, *ApJ*, 329, 702  
 Krolik, J. H., & Kriss, G. A. 1995, *ApJ*, 447, 512  
 ———. 2001, *ApJ*, 561, 684  
 Krongold, Y., Nicastro, F., Brickhouse, N. S., Elvis, M., Liedahl, D. A., & Mathur, S. 2003, *ApJ*, 597, 832  
 Lamers, H. J. G. L. M., & Cassinelli, J. P. 1999, *Introduction to Stellar Winds* (Cambridge: Cambridge Univ. Press)  
 Lang, K. R. 1999, *Astrophysical Formulae* (New York: Springer)  
 Laor, A. 1998, *ApJ*, 496, L71

- Lee, J. C., Ogle, P. M., Canizares, C. R., Marshall, H. L., Schulz, N. S., Morales, R., Fabian, A. C., & Iwasawa, K. 2001, *ApJ*, 554, L13
- Murray, N., Chiang, J., Grossman, S. A., & Voit, G. M. 1995, *ApJ*, 451, 498
- Netzer, H. 2004, *ApJ*, 604, 551
- Netzer, H., Chelouche, D., George, I. M., Turner, T. J., Crenshaw, D. M., Kraemer, S. B., & Nandra, K. 2002, *ApJ*, 571, 256
- Netzer, H., et al. 2003, *ApJ*, 599, 933 (N03)
- Parker, E. N. 1958, *ApJ*, 128, 664
- Peterson, B. M., et al. 2004, *ApJ*, 613, 682
- Porquet, D., Reeves, J. N., O'Brien, P., & Brinkmann, W. 2004, *A&A*, 422, 85
- Reeves, J. N., Nandra, K., George, I. M., Pounds, K. A., Turner, T. J., & Yaqoob, T. 2004, *ApJ*, 602, 648
- Reynolds, C. S., & Fabian, A. C. 1995, *MNRAS*, 273, 1167
- Scannapieco, E., & Oh, S. P. 2004, *ApJ*, 608, 62
- Schödel, R., Ott, T., Genzel, R., Eckart, E., Mouawad, N., & Alexander, T. 2003, *ApJ*, 596, 1015
- Scoville, N., & Norman, C. 1995, *ApJ*, 451, 510
- Shemmer, O., Netzer, H., Maiolino, R., Oliva, E., Croom, S., Corbett, E., & di Fabrizio, L. 2004, *ApJ*, 614, 547
- Shu, F. H. 1992, *Physics of Astrophysics*, Vol. 2 (Mill Valley: University Science Books)
- Steenbrugge, K. C., et al. 2005, *A&A*, in press (astro-ph/0501122)
- Woods, D. T., Klein, R. F., Castor, J. I., McKee, C. F., & Bell, J. B. 1996, *ApJ*, 461, 767